Effects of Finite Rf Pulses and Sample Spinning Speed in Multiple-Quantum Magic-Angle Spinning (MQ-MAS) and Multiple-Quantum Quadrupolar Carr−Purcell−Meiboom−Gill Magic-Angle Spinning (MQ-QCPMG-MAS) Nuclear Magnetic Resonance of Half-Integer Quadrupolar Nuclei

Flemming H. Larsen[†] **and Niels Chr. Nielsen***

Laboratory for Biomolecular NMR Spectroscopy, Department of Molecular and Structural Biology, Science Park, University of Aarhus, DK-8000 Aarhus C, Denmark

Received: August 9, 1999; In Final Form: September 29, 1999

The multiple-quantum magic-angle spinning (MQ-MAS) solid-state nuclear magnetic resonance (NMR) experiment and a sensitivity-enhanced variant detecting the second-order quadrupolar powder pattern through a train of quadrupolar Carr−Purcell−Meiboom−Gill refocusing pulses (MQ-QCPMG-MAS) are analyzed with respect to the effects of finite radio frequency (rf) pulse irradiation and the MAS frequency. Taking these effects explicitly into account, it is possible to accurately determine optimum conditions for excitation of MQ coherences and reconversion of these into detectable single-quantum coherences as well as simulate the second-order quadrupolar lineshape necessary to extract accurate parameters for quadrupolar coupling interactions and isotropic chemical shifts. This accurate determination is of great importance for the exploitation of MQ-MAS and MQ-QCPMG-MAS NMR experiments for quantitative determination of site populations. The various effects are described analytically and demonstrated by numerical simulations and by ^{87}Rb MQ-MAS and MQ-QCPMG-MAS experiments on $RbNO_3$.

1. Introduction

Since its introduction in 1995, the multiple-quantum magic-angle spinning (MQ-MAS) experiment[1] has attracted widespread interest as a method to obtain high-resolution spectra of half-integer quadrupolar nuclei. Contributing to this success has been the fact that MQ-MAS experiments relative to the previous dynamic-angle spinning (DAS)[2−4] and double rotation (DOR)[3,5,6] experiments do not require sophisticated experimental equipment. Furthermore, MQ-MAS is not limited by the demand of long T_1 relaxation times (DAS) or limitations in the spinning frequencies easily met under DOR conditions. In addition to these obvious advantages, the 2-dimensional (2D) MQ-MAS experiment provides information about the second-order quadrupolar shifted isotropic chemical shifts in the high-resolution dimension correlated to second-order quadrupolar powder patterns in the other dimension. This information allows the establishment of structurally important information about the electric field gradients for the individual sites and through this knowledge about the isotropic chemical shifts from the high-resolution dimension of the MQ-MAS spectra.

With the positive aspects of the MQ-MAS experiment stated, it is relevant to consider a number of practical difficulties also present for this method. These difficulties have motivated the large number of the papers published on MQ-MAS nuclear magnetic resonance (NMR). The first and most obvious problem is the low transfer efficiencies associated with excitation of MQ coherences and the following reconversion of these into detectable single-quantum (1Q) coherence. These efficiencies highly depend on the magnitude of the quadrupolar coupling tensor, the radio frequency (rf) field strength, and the sample spinning frequency, which effectively sets an upper limit on the quadrupolar coupling constant (C_Q) for the nuclei amenable for analysis by MQ-MAS NMR. Furthermore, the strong dependence on C_Q may severely complicate application of MQ-MAS for quantitative determination of site populations. To improve the sensitivity and the conditions for quantitative measurements, the original three-pulse sequence has been modified to involve single-pulse MQ excitation,[7−9] spin-lock type excitation and mixing (RIACT),[10,11] composite pulses,[12] shaped pulses,[13] and adiabatic or phase-modulated pulses.[14,15] By these methods, the sensitivity of MQ-MAS experiments has been improved by a factor of up to about four. A second problem is the detection of the MQ-MAS spectra via second-order quadrupolar broadened powder lineshapes. To cope with this problem we recently introduced the MQ-QCPMG-MAS experiment[16] which by detection of the signal in course of a quadrupolar Carr−Purcell−Meiboom−Gill (QCPMG)[17,18] train of refocusing pulses effectively splits the second-order powder pattern into a manifold of narrow spin-echo sidebands.[19−21] In this manner, the sensitivity of the MQ-MAS experiment may be improved by an order of magnitude while maintaining information about the anisotropic interactions.

Despite these achievements, the general utility of MQ-MAS still critically relies on specific details on the quantum evolution taking place during periods of free precession and finite rf pulse irradiation under consideration of MAS. This covers the feasibility of the experiment considering actual C_Q values and available rf field strengths, quantitative measurements, and extraction of reliable quadrupolar coupling and chemical shielding parameters to characterize the individual sites. In this work we analyze MQ-MAS and MQ-QCPMG-MAS experiments with respect to finite rf pulses and sample spinning conditions. This

---

* Corresponding author. Fax: +4586 196199. Telephone: +4589 423841. E-mail: ncn@kemi.aau.dk.

[†] Present address: Danfoss A/S, DK-6430 Nordborg, Denmark.

10.1021/jp992798i CCC: $18.00

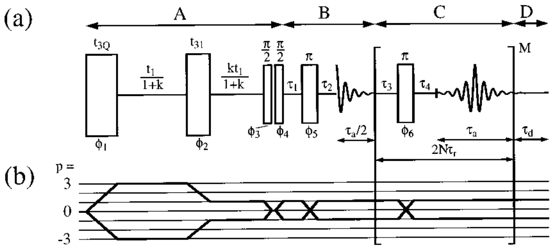

Figure 1. (a) Timing diagram for the MQ-QCPMG-MAS pulse sequence[16] with the periods A, B, C, and D designating a *z*-filtered MQ-MAS sequence, a QE sequence, the *M*-time replicating part of a QCPMG sequence, and an additional sampling period to ensure full decay of the FID, respectively. The rf pulse durations (t_{3Q} and t_{31}) or nominal flip-angles are given above the pulses, and their phases are given below the pulses. *M* denotes the number of refocusing pulses in pulse train. The pulse sequence is rotor synchronized to ensure coincident spin and rotor echoes using $\tau_1 = \tau_r - t_{3\pi/4}$, $\tau_2 = \tau_r - t_{\pi/2}$, and $2N\tau_r = \tau_3 + \tau_4 + t_\pi + \tau_a$, where *N* is an integer and t_θ the length of a pulse with flip angle θ. (b) The coherence transfer pathway selected by phase cycling as described in refs 19 and 32: $\phi_i = \phi_i^\circ + 2\pi j/N_i$, with $j = 0, ..., N_i - 1$ and N_i representing the number of steps 6, 4, 2, 2, 1, and 2 for $i = 1, 2, 3, 4, 5$, and 6, respectively, and the receiver reference phase adjusted to select the coherences indicated, according to standard procedures.[43] $\phi_1^\circ = \phi_2^\circ = \phi_3^\circ = \phi_4^\circ = 0$ and $\phi_5^\circ = \phi_6^\circ = \pi/2$.

work leads to optimum conditions for the excitation and mixing pulses (which is particularly important if only moderate rf fields strengths are available) being different from and considerably better than those attained following established rules. Furthermore, this work enables accurate simulation of second-order powder or spin-echo sideband spectra detected in the anisotropic dimension of MQ-MAS and MQ-QCPMG-MAS experiments. On basis of the experimental parameters and quadrupolar coupling parameters established through iterative fitting, it is possible to determine isotropic chemical shifts and extract accurate information about site populations. These aspects are demonstrated by ^{87}Rb MQ-MAS and MQ-QCPMG-MAS NMR spectra of RbNO$_3$.

2. Theory

The response of an ensemble of half-integer quadrupolar nuclei to MQ-MAS and MQ-QCPMG-MAS NMR experiments (Figure 1) may be described in the Zeeman interaction representation by the high-field truncated effective Hamiltonian

$$\bar{\tilde{H}}(t) = \bar{\tilde{H}}_{\rm int}(t) + \tilde{H}_{\rm rf} \tag{1}$$

$$\bar{\tilde{H}}_{\rm int}(t) = \bar{\tilde{H}}{}_\delta^{\rm iso} + \bar{\tilde{H}}{}_{\rm Q}^{(1)}(t) + \bar{\tilde{H}}{}_{\rm Q}^{(2)}(t) \tag{2}$$

where

$$\tilde{H}_{\rm rf} = \omega_{\rm rf}(I_x \cos\phi + I_y \sin\phi) \tag{3}$$

$$\bar{\tilde{H}}{}_\delta^{\rm iso} = -\omega_0 \delta_{\rm iso} I_z \tag{4}$$

$$\bar{\tilde{H}}{}_{\rm Q}^{(1)}(t) = 2\omega_{\rm Q}(R_{2,0}^{\rm Q})^L T_{2,0}^{\rm Q} \tag{5}$$

$$\bar{\tilde{H}}{}_{\rm Q}^{(2)}(t) = -\frac{2{\omega_{\rm Q}}^2}{\omega_0}(2(R_{2,-1}^{\rm Q})^L(R_{2,1}^{\rm Q})^L[T_{2,1}^{\rm Q}, T_{2,-1}^{\rm Q}] + (R_{2,-2}^{\rm Q})^L(R_{2,2}^{\rm Q})^L[T_{2,2}^{\rm Q}, T_{2,-2}^{\rm Q}]) \tag{6}$$

describe rf irradiation of amplitude $\omega_{\rm rf} = -\gamma B_{\rm rf}$ and phase ϕ, isotropic chemical shift, and the secular part of the quadrupolar coupling interaction to first and second order, respectively. The terms $\omega_0 = -\gamma B_0$, $\delta_{\rm iso}$, $\omega_{\rm Q} = 2\pi C_{\rm Q}/(4I(2I - 1))$, and $C_{\rm Q} = e^2qQ/h$ denote the Larmor frequency, the isotropic chemical shift, the quadrupole splitting, and the quadrupole coupling constant, respectively. The parameter *I* is the spin quantum number. Effects from anisotropic chemical shielding and dipolar coupling as well as relaxation are ignored in the present analysis.

The relevant irreducible spin tensor operators are related to Cartesian spin operators as

$$T_{2,0}^{\rm Q} = \frac{1}{\sqrt{6}}(3{I_z}^2 - I(I + 1)) \tag{7}$$

$$[T_{2,1}^{\rm Q}, T_{2,-1}^{\rm Q}] = \frac{1}{2}I_z(4I(I + 1) - 8{I_z}^2 - 1) \tag{8}$$

$$[T_{2,2}^{\rm Q}, T_{2,-2}^{\rm Q}] = I_z(2I(I + 1) - 2{I_z}^2 - 1) \tag{9}$$

The irreducible spatial tensors may conveniently be written

$$(R_{2,m}^{\rm Q})^{\rm L} = \sum_{m''=-2}^{2}\sum_{m'=-2}^{2}(R_{2,m''}^{\rm Q})^{\rm P}\,{\rm e}^{-{\rm i}m''\alpha_{\rm PR}}\mathbf{d}_{m'',m'}^{(2)}(\beta_{\rm PR}) \times \mathbf{d}_{m',m}^{(2)}(\beta_{\rm RL}){\rm e}^{-{\rm i}m'(\gamma_{\rm PR}+\omega_{\rm r}t)} \tag{10}$$

where $(R_{2,0}^{\rm Q})^{\rm P} = \sqrt{3/2}$, $(R_{2,\pm1}^{\rm Q})^{\rm P} = 0$, and $(R_{2,\pm2}^{\rm Q})^{\rm P} = \eta_{\rm Q}/2$ are spatial elements of the quadrupolar coupling tensor (asymmetry parameter $\eta_{\rm Q}$) in the principal axis frame (P). The parameter $\mathbf{d}^{(2)}$ is a reduced Wigner matrix, and $(\alpha_{\rm PR},\beta_{\rm PR},\gamma_{\rm PR})$ and $(\omega_{\rm r}t,\beta_{\rm RL},0)$ denote Euler angles for the transformation from P to the rotor frame (R) and from R to the laboratory frame (L), respectively, with $\omega_{\rm r}$ being the angular sample spinning frequency.

To obtain analytical insight and an expression for the isotropic shift in the $\omega_1/2\pi$ dimension of the MQ-MAS experiment, it proves convenient to rewrite $\bar{\tilde{H}}{}_{\rm Q}^{(2)}(t)$ as[22]

$$\bar{\tilde{H}}{}_{\rm Q}^{(2)} = \frac{I_z}{70}\{28\sqrt{5}V_{00}(3{I_z}^2 - I(I + 1)) + 5\sqrt{14}V_{20}(8I(I + 1) - 12{I_z}^2 - 3) + \sqrt{70}V_{40}(18I(I + 1) - 34{I_z}^2 - 5)\} \tag{11}$$

using

$$\begin{aligned} V_{j0} &= -\frac{2{\omega_{\rm Q}}^2}{\omega_0}\sum_{n=0}^{2}C(22j; -nn)(R_{2,-n}^{\rm Q})^{\rm L}(R_{2,n}^{\rm Q})^{\rm L} \\ &= \sum_{k=-j}^{j}A_{jk}(\eta_{\rm Q})\sum_{n=-j}^{j}{\rm e}^{-{\rm i}k\alpha_{\rm PR}}\mathbf{d}_{kn}^{(j)}(\beta_{\rm PR}){\rm e}^{-{\rm i}n(\gamma_{\rm PR}+\omega_{\rm r}t)}\mathbf{d}_{n0}^{(j)}(\beta_{\rm RL}) \end{aligned} \tag{12}$$

with

$$A_{jk}(\eta_{\rm Q}) = -\frac{2{\omega_{\rm Q}}^2}{\omega_0}\sum_{n=0}^{2}C(22j; -n(n - k))(R_{2,-n}^{\rm Q})^{\rm P}(R_{2,(n-k)}^{\rm Q})^{\rm P} \tag{13}$$

where $C(22j; pq)$ denotes a Clebsh−Gordan coefficient.[23]

Restricting focus to the lineshape of the centerband being sufficient using high-speed MAS, it is relevant to consider only the time-independent parts of V_{j0} with $n = 0$; that is,

$$V'_{j0} = \mathbf{d}_{00}^{(j)}(\beta_{\rm RL})\sum_{k=-j}^{j}A_{jk}(\eta_{\rm Q}){\rm e}^{-{\rm i}k\alpha_{\rm PR}}\mathbf{d}^{(j)}{}_{k0}(\beta_{\rm PR}) \tag{14}$$

where $\mathbf{d}_{00}^{(j)}(\beta_{\rm RL})$ correspond to the $j^{\rm th}$ degree Legendre polynomials: $\mathbf{d}_{00}^{(0)}(\beta_{\rm RL}) = 1$, $\mathbf{d}_{00}^{(2)}(\beta_{\rm RL}) = {}^1/_2(3\cos^2(\beta_{\rm RL}) - 1)$, and $\mathbf{d}_{00}^{(4)}(\beta_{\rm RL}) = {}^1/_8(35\cos^4(\beta_{\rm RL}) - 30\cos^2(\beta_{\rm RL}) + 3)$. It is evident that V_{00} is an isotropic shift induced by the second-order quadrupolar coupling interaction and that V'_{20} is eliminated by adjusting β_{RL} to the magic angle.

The remaining anisotropic term

$$\tilde{\bar{H}}_{40} = \frac{V'_{40}}{\sqrt{70}} I_z(18I(I+1) - 34I_z^{\,2} - 5) \qquad (15)$$

may be eliminated using MQ-MAS.[1] This result becomes evident by considering the anisotropic transition frequency for the m-quantum $(m/2,-m/2)$ transition,

$$\begin{aligned}\omega'_{\mathrm{Q}}(m/2,-m/2) &= \left\langle -\frac{m}{2}\right|\tilde{\bar{H}}_{40}\left|-\frac{m}{2}\right\rangle - \left\langle\frac{m}{2}\right|\tilde{\bar{H}}_{40}\left|\frac{m}{2}\right\rangle \\ &= -\frac{mV'_{40}}{\sqrt{70}}\left(18I(I+1) - \frac{17m^2+10}{2}\right) \qquad (16)\end{aligned}$$

revealing that $\tilde{\bar{H}}_{40}$ may be averaged by evolution of m-quantum coherence in a period $t_1/(1+k)$ followed by evolution of 1Q coherence in a period $kt_1/(1+k)$ with

$$k = \frac{\omega'_{\mathrm{Q}}(m/2,-m/2)}{\omega'_{\mathrm{Q}}(1/2,-1/2)} = -\frac{m(36I(I+1) - 17m^2 - 10)}{36I(I+1) - 27} \qquad (17)$$

This condition leaves us with

$$\tilde{\bar{H}}_{\mathrm{iso}} = -I_z\left(\delta_{\mathrm{iso}}\omega_0 + \frac{2\omega_{\mathrm{Q}}^{\,2}}{5\omega_0}(3+\eta_{\mathrm{Q}}^{\,2})(3I_z^{\,2} - I(I+1))\right) \qquad (18)$$

describing evolution under the isotropic parts of the chemical shielding and second-order quadrupolar coupling interactions during the t_1 period of the MQ-MAS experiment.

The isotropic shift δ'_{iso} in the $\omega_1/2\pi$ dimension may be calculated as

$$\begin{aligned}\delta'_{\mathrm{iso}} &= -\frac{1}{\omega_0(1+k)}\left(k\left\{\left\langle\frac{1}{2}\right|\tilde{\bar{H}}_{\mathrm{iso}}\left|\frac{1}{2}\right\rangle - \left\langle-\frac{1}{2}\right|\tilde{\bar{H}}_{\mathrm{iso}}\left|-\frac{1}{2}\right\rangle\right\} + \right. \\ &\qquad \left.\left\langle\frac{m}{2}\right|\tilde{\bar{H}}_{\mathrm{iso}}\left|\frac{m}{2}\right\rangle - \left\langle-\frac{m}{2}\right|\tilde{\bar{H}}_{\mathrm{iso}}\left|-\frac{m}{2}\right\rangle\right) \\ &= \frac{1}{1+k}\left(\delta_{\mathrm{iso}}(k+m) + \frac{8\omega_{\mathrm{Q}}^{\,2}}{5\omega_0^{\,2}}(3+\eta_{\mathrm{Q}}^{\,2})(3(k+m^3) - \right. \\ &\qquad \left. 4(k+m)I(I+1))\right) \qquad (19)\end{aligned}$$

We note that δ_{iso} and $\omega_{\mathrm{Q}}^2(3+\eta_{\mathrm{Q}}^2)$ may be determined from the isotropic shifts $\delta'_{\mathrm{iso},1}$ and $\delta'_{\mathrm{iso},2}$ determined in two experiments with different Larmor frequencies of $\omega_{0,1}$ and $\omega_{0,2}$, respectively:

$$\delta_{\mathrm{iso}} = \frac{k+1}{k+m}\left\{\delta'_{\mathrm{iso},1} + \frac{\omega_{0,2}^{\,2}(\delta'_{\mathrm{iso},2} - \delta'_{\mathrm{iso},1})}{\omega_{0,2}^{\,2} - \omega_{0,1}^{\,2}}\right\} \qquad (20)$$

$$\omega_{\mathrm{Q}}^{\,2}(3+\eta_{\mathrm{Q}}^{\,2}) = \frac{5(1+k)\omega_{0,1}^{\,2}\omega_{0,2}^{\,2}(\delta_{\mathrm{iso},2} - \delta'_{\mathrm{iso},1})}{8\{3(k+m^3) - 4(k+m)I(I+1)\}(\omega_{0,1}^{\,2} - \omega_{0,2}^{\,2})} \qquad (21)$$

More practically, δ_{iso} may be determined from a single experiment by simulation of traces in the anisotropic information of the 2D experiment or using δ'_{iso} in combination with values for C_{Q} and η_{Q} established from this dimension.

Equipped with the Hamiltonians described by eqs 1−10, it is feasible to numerically calculate the response of an ensemble of half-integer quadrupolar nuclei to the MQ-MAS and MQ-QCPMG-MAS pulse sequences in Figure 1. Both experiments employ z-filtering to balance the evolution of 1Q and MQ coherences and thereby facilitate the attainment of pure absorption spectra without the need for shearing transformations[24−26] and, more importantly in the present context, combination with quadrupolar-echo (QE)[27−29] type refocusing sequences. The MQ-QCPMG-MAS sequence[16] is composed of four elements: part A represents a z-filtered MQ-MAS sequence, part B is a rotor-synchronized QE sequence with sampling of the decaying part of the echo, part C is an M-time repeating unit constituting the QCPMG train of rotor-synchronized refocusing pulses during which the signal is sampled, and part D is an additional sampling period ensuring full decay of the signal. The z-filtered MQ-MAS pulse sequence with detection following a quadrupolar echo (MQ-QE-MAS) is formed by parts A and B of the pulse sequence alone. The relevant coherence transfer pathway is given below the timing diagram of the pulse sequence in Figure 1.

Within the secular approximation, the propagator describing the spin evolution in the period from t_1 to t_2 takes the general form

$$\tilde{U}(t_2,t_1) = T\exp\{-\mathrm{i}\int_{t_1}^{t_2}\tilde{\bar{H}}(t)\,\mathrm{d}t\} \qquad (22)$$

depending on the Hamiltonian in eq 1 with $\omega_{\mathrm{rf}} = 0$ and $\omega_{\mathrm{rf}} \neq 0$ for periods without and with rf irradiation, respectively. The parameter T is a Dyson time-ordering operator[30] necessary in the latter case because $[\tilde{\bar{H}}(t'), \tilde{\bar{H}}(t'')] \neq 0$. In periods of free precession, the Hamiltonian is diagonal and the propagator is formed by direct integration. During rf pulses, the Hamiltonian is tridiagonal and the propagator is obtained as a time-ordered product of propagators, each corresponding to a time interval over which the Hamiltonian may be considered time independent.[21] With the reduced density operator at any time t during the pulse sequence expressed as

$$\tilde{\rho}(t) = \tilde{U}(t,0)\,\tilde{\rho}(0)\,\tilde{U}^{\dagger}(t,0) \qquad (23)$$

where $\tilde{\rho}(0) = I_z$ represents the initial equilibrium polarization, the free induction decay (FID) for a powder sample takes the form

$$s(t) = \frac{1}{8\pi^2}\int_0^{2\pi}\mathrm{d}\alpha_{\mathrm{CR}}\int_0^{\pi}\sin(\beta_{\mathrm{CR}})\,\mathrm{d}\beta_{\mathrm{CR}}\int_0^{2\pi}\times \mathrm{d}\gamma_{\mathrm{CR}}\,\mathrm{Tr}\{I^{+}\,\tilde{\rho}(t)\} \qquad (24)$$

with I^{+} being an representative of the ‘observable’ operator under quadrature detection.

3. Experimental

All ^{87}Rb MQ-QE-MAS and MQ-QCPMG-MAS spectra were recorded on a narrow-bore (51 mm) Varian INOVA 300 (7.05 T; 98.14 MHz for ^{87}Rb) spectrometer equipped with a home-built MAS probe using 7 mm PSZ (partially stabilized zirconia) rotors. The experiments employed a MAS frequency of $\omega_{\mathrm{r}}/2\pi = 4808$ Hz stabilized to ±2 Hz using a Varian spinning speed controller. An rf field strength of $\omega_{\mathrm{rf}}/2\pi = 50$ kHz was used for the excitation and reconversion pulses, whereas the strength was $\omega_{\mathrm{rf2}}/2\pi = 25.6$ kHz for the z-filter and refocusing pulses. The 2D spectra were recorded using 192 scans (0.5 s relaxation delay) for each of the 96 t_1 increments taken in steps of 20 μs.

Pure absorption spectra were obtained using the hypercomplex method as described by Massiot et al.[32] The time-domain signals were zero-filled to 2048 (t_1) × 32 768 (t_2) complex points prior to 2D Fourier transformation. The ^{87}Rb chemical shifts were referenced to an external 1 M aqueous solution of $RbNO_3$. Numerical simulations and iterative fitting were performed on a 450 MHz Pentium III computer using procedures similar to those described in refs 19 and 21. The simulations used powder averaging with 987 (QCPMG) or 4181 (QE) pairs $\{\alpha_{CR},\beta_{CR}\}$ angles distributed according to the tiling scheme of Zaremba[31] and 20 equidistantly distributed γ_{CR} angles. Integration of the homogeneous evolution during rf pulses (i.e., Dyson time ordering) was accomplished in steps of 0.5 μs. A typical simulation of a $\omega_2/2\pi$ trace, taking into account finite rf pulse effects, required 107 and 68 min (24.3 min) of computation time for MQ-QE-MAS and MQ-QCPMG-MAS experiments, respectively. The number in the parenthesis refers to simplified simulations taking finite pulses into account by replication of the FID sampled in part C of the pulse sequence.

4. Results and Discussion

As discussed by several authors, the sensitivity of the MQ-MAS experiment for spin $I = 3/2$ nuclei critically depends on appropriate excitation of of triple-quantum (3Q) coherence and subsequent reconversion of this into observable 1Q coherence.[7,12,33] In the simplest approach, both the 3Q excitation and the 3Q-to-1Q reconversion may be accomplished by single rf pulses[7-9] exploiting finite pulse effects.[34-36] Sequences of this type benefit from straightforward performance and relatively high sensitivity under favorable conditions. Unfortunately, however, the efficiency is highly dependent on the magnitude of the quadrupolar coupling interaction for the individual sites relative to the applied rf field strength as well as the sample spinning frequency. To analyze these aspects and to optimize the parameters for the MQ-MAS and MQ-QCPMG-MAS experiments described in the following, Figures 2 and 3 contain curves for +3Q excitation and +3Q-to-+1Q reconversion, respectively, calculated for single rf pulses with quadrupolar splitting to rf field strength ratios ($|\omega_Q/\omega_{rf}|$) of 1, 2, 3, and 4 ($C_Q = 2.4$ MHz) and sample spinning frequencies ($\omega_r/2\pi$) of 0 (static), 5, 10, and 20 kHz. Specifically, the excitation curves display the imaginary part of $\tilde{\rho}_{1,4}$ (i.e., +3Q coherence) as function of the pulse width t_{3Q} (cf. Figure 1), whereas the reconversion curves (based on the optimum excitation efficiency) depict the imaginary part of $\tilde{\rho}_{3,2}$ (i.e., +1Q coherence) after the z-filter as function of t_{31}. The curves, which describe the spin evolution over one or more rotor periods, are calculated by explicitly taking into account the sample spinning in course of the rf pulses.[35,36]

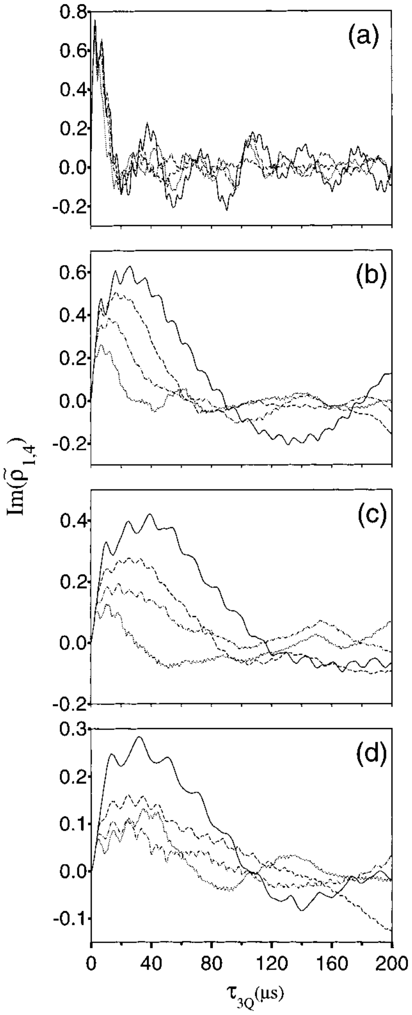

Figure 2. Efficiencies for transfer of I_z into $+3Q$ coherence (imaginary part of $\tilde{\rho}_{1,4}$) versus the pulse length t_{3Q} (cf. Figure 1). The curves reflect $|\omega_Q/\omega_{rf}|$ ratios of (a) 1, (b) 2, (c) 3, and (d) 4 using $C_Q = 2.4$ MHz and $\eta_Q = 0$ and spinning frequencies of 0 (solid line), 5 (dashed line), 10 (dot-dashed line), and 20 (dotted line) kHz.

In accord with previous findings,[7,33] it is seen that both the +3Q excitation and the +3Q-to-+1Q reconversion are favored using the strongest possible rf field strength under slow-speed spinning conditions. This result may imply a compromise to be taken between sensitivity and resolution, although typically taken in the favor of a reasonably high sample spinning frequency. Overlap between the centerband and the spinning sidebands in the $\omega_2/2\pi$ dimension of the 2D spectrum is undesirable not only for sensitivity reasons but also because it may complicate extraction of information about the anisotropic interactions. Spinning sidebands in the isotropic $\omega_1/2\pi$ dimension are not desired for sensitivity reasons. Obviously, the latter problem may be alleviated by rotor synchronization.[37] From the excitation/reconversion profiles in Figures 2 and 3 it becomes clearly evident that it is worthwhile considering the spin evolution over one or more rotor periods. This consideration appears relevant for both pulses in the regime of large quadrupolar couplings relative to the rf field strength (i.e., $|\omega_Q/\omega_{rf}| > 2$) and in particular for the 3Q-to-1Q reconversion pulse, which even in the case of relatively large rf field strengths may be as long as $\tau_r/4$ to $3\tau_r/4$ ($\tau_r = 2\pi/\omega_r$). This recommendation is in marked contrast to those prevailing in the literature. For example, using similar rf irradiation and quadrupolar coupling parameters and explicit integration of the spin evolution during the rf pulses, Wu et al.[7] found maximum reconversion for much shorter rf pulses with flip angles of the order 45−60°. It is noted that we arrived at similar results when transforming a mixture of −3Q and +3Q (as generated by an optimum 3Q excitation pulse) into +1Q coherence (not shown). Among these transfers, however, only the +3Q-to-+1Q transfer causes refocusing of the second-order quadrupolar coupling interaction. Several practically important features can be extracted from the curves in Figures 2 and 3. First, it appears that by using appropriately long excitation and reconversion pulses, it is possible to considerably enhance the sensitivity of the MQ-MAS experiments relative to what was achieved using commonly recommended pulse lengths. Using this approach, however, it should be realized that anisotropies in the excitation and reconversion processes potentially may cause a considerable distortion of the

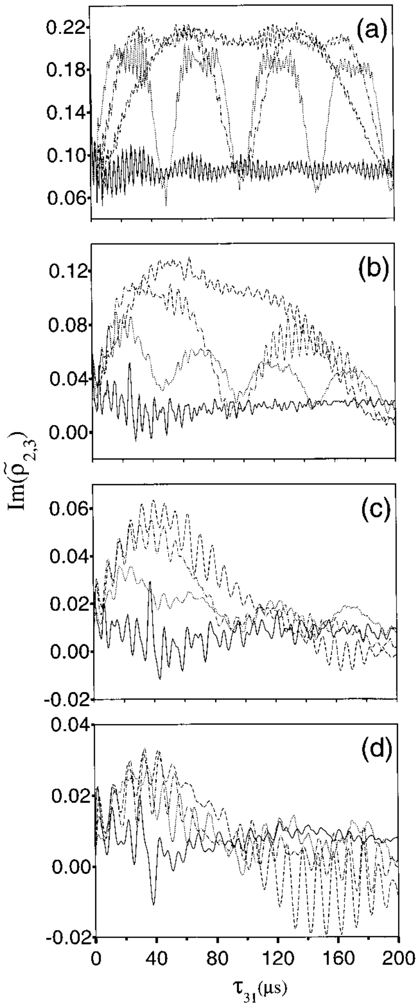

Figure 3. Efficiencies for transfer of +3Q coherence to +1Q (imaginary part of $\tilde{\rho}_{2,3}$) coherence versus the pulse length t_{31} (cf. Figure 1). The 3Q-to-1Q transfer efficiencies are based on the optimum +3Q operator determined from the excitation profiles in Figure 2. The curves reflect $|\omega_Q/\omega_{rf}|$ ratios of (a) 1, (b) 2, (c) 3, and (d) 4 using $C_Q = 2.4$ MHz and $\eta_Q = 0$ and spinning frequencies of 0 (solid line), 5 (dashed line), 10 (dot-dashed line), and 20 (dotted line) kHz. Optimum t_{3Q} pulses for the various spin rates (in parenthesis) and rf field strength were (a) 3.5 μs for all spinning frequencies; (b) 26.5 (static), 17.5 (5 kHz), 12.5 (10 kHz), and 7.5 (20 kHz) μs; (c) 40.0 (static), 25.5 (5 kHz), 18.5 (10 kHz), and 11.0 μs (20 kHz); and (d) 32.5 (static), 25.0 (5 kHz), 24.0 (10 kHz), and 35.5 μs (20 kHz).

second-order powder patterns observed in the $\omega_2/2\pi$-dimension of the 2D spectrum. This distortion calls for explicit evaluation of finite rf pulse effects to extract information about the quadrupolar coupling parameters. Second, with appropriate knowledge on the quadrupolar interaction parameters (determined from the $\omega_2/2\pi$ dimension of the 2D spectrum), it is possible to determine the relative site populations. Both aspects reinforce the need for explicit evaluation of finite rf pulse effects in simulation of MQ-MAS spectra.

Figures 4 and 5 show ^{87}Rb MQ-QE-MAS and MQ-QCPMG-MAS spectra, respectively, of $RbNO_3$ obtained using the pulse sequence in Figure 1 with a modest rf field strength of $\omega_{rf}/2\pi = 50$ kHz for the excitation and reconversion pulses with optimized pulse lengths of $t_{3Q} = 35$ μs and $t_{31} = 42$ μs, respectively. For the ^{87}Rb sites in $RbNO_3$ this modest rf field strength correspond to $|\omega_Q/\omega_{rf}|$ values in the region of 2.8 to 3.3. A relatively weak rf field ($\omega_{rf2}/2\pi = 25.6$ kHz) was used for the *z*-filter and refocusing pulses. This weak rf field strength corresponds to $|\omega_Q/\omega_{rf2}| > 5$ and $2\omega_Q^2/(\omega_0\omega_{rf2}) \approx 0.02$ which, with the relevant pulse widths scaled by a factor of $(I + {}^1/_2)^{-1}$, ensures selective operation on the $({}^1/_2,-{}^1/_2)$ central transition. The contour plots and the adjacent projections display the typical correlation of high-resolution isotropic peaks in the $\omega_1/2\pi$ dimension with second-order quadrupolar powder patterns (Figure 4) or spin-echo sideband manifolds (Figure 5) in the $\omega_2/2\pi$ dimension. Comparing the sensitivity of the two spectra reveals a gain by a factor of 12 (corresponding to a factor of 144 in spectrometer time) for the MQ-QCPMG-MAS spectrum obtained by splitting the powder pattern into sidebands by detection through a QCPMG train of central-transition selective refocusing pulses. The actual gain in sensitivity obviously depends on the sideband separations in the $\omega_1/2\pi$ dimension (and thereby on τ_a), allowing compromises to be taken between sensitivity and details in the information about the anisotropic spin interactions.

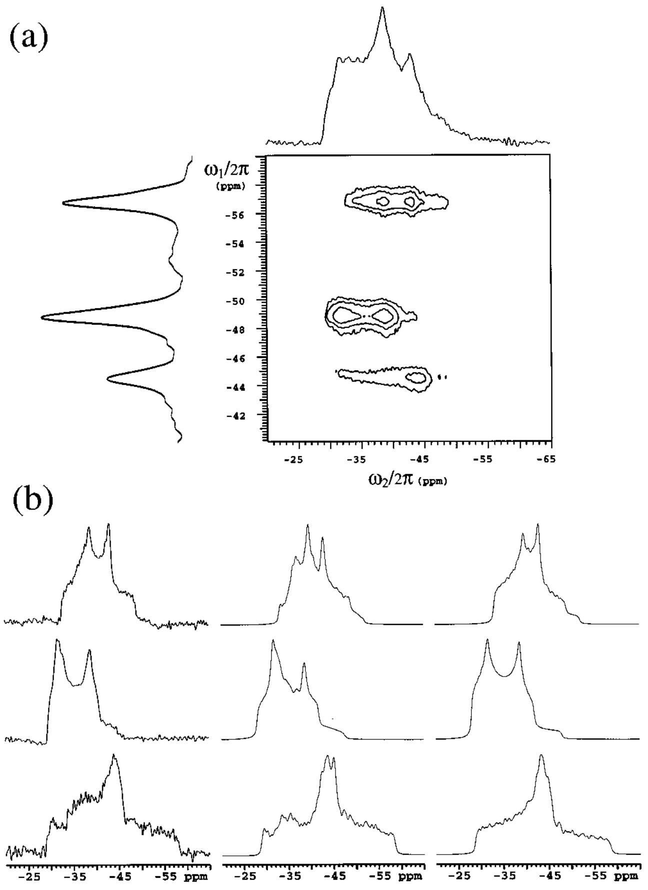

Figure 4. Experimental and simulated ^{87}Rb MQ-QE-MAS spectra of $RbNO_3$. The experimental 2D spectrum shown in (a) along with projections onto the $\omega_1/2\pi$ (vertical) and $\omega_2/2\pi$ (horizontal) axes was recorded using the pulse sequence in Figure 1 (parts A and B only) with $\omega_{rf}/2\pi = 50$ kHz, $\omega_{rf2}/2\pi = 25.6$ kHz, $\omega_r/2\pi = 4808$ Hz, $\tau_1 = 200.7$ μs, $\tau_2 = 203.1$ μs, $t_\pi = 9.75$ μs, and optimum pulse widths $t_{3Q} = 35.0$ μs and $t_{31} = 42.0$ μs. The 2D spectrum was obtained using 192 scans for each of the 96 t_1-increments with dwell times of 20.0 and 142.9 μs in the t_1 and t_2 dimensions, respectively. The spectrum was apodized by Lorentzian linebroadenings of 1 and 5 Hz in the isotropic and anisotropic dimensions, respectively. (b) $\omega_2/2\pi$ traces through the three $\omega_1/2\pi$ resonances of the experimental spectrum (left column) along with numerical simulations (center column) using parameters obtained by iterative fitting of the corresponding $\omega_2/2\pi$ traces from the MQ-QCPMG-MAS spectrum in Figure 5 (parameters in Table 1). For comparison, the right column includes simulations using the same parameters as the center column but calculated under the assumption of ideal single-pulse excitation.

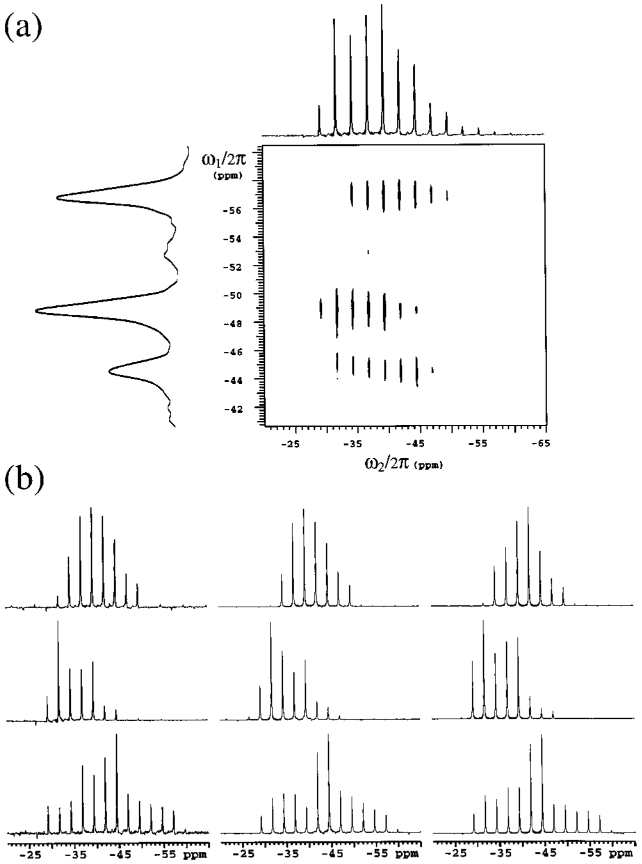

Figure 5. Experimental and simulated ^{87}Rb MQ-QCPMG-MAS NMR spectra of RbNO$_3$. The parameters and layout of the figure is identical to Figure 4 with the exception that the experimental spectrum was recorded using the full pulse sequence in Figure 1 with the additional parameters $\tau_3 = \tau_4 = 75.0\ \mu$s, $\tau_a = 4.0$ ms, $M = 19$, and $\tau_d = 3.92$ ms. Furthermore, the spectrum was apodized by 1 Hz Lorentzian line-broadening in both dimensions.

To extract information on the electric field gradients and the chemical shifts, both reflecting the local electronic environment of the quadrupolar nuclei, as well as reliable quantitative information about site populations, it is fundamental to determine parameters for the anisotropic interactions from $\omega_2/2\pi$ sections through the various isotropic $\omega_1/2\pi$ resonances. In favorable cases, this information may, at least approximately, be extracted by simulation of the $\omega_2/2\pi$ sections using standard programs for calculation of second-order quadrupolar powder spectra resulting from ideal excitation.[8,32,39] In more general cases, using finite pulses with rf field strengths in the region of $1 < |\omega_Q/\omega_{rf}| < 3$ and with durations extending over a significant fraction of the rotor period,[35] the transfer efficiency may vary significantly for the various crystallite orientations causing distortion of the $\omega_2/2\pi$ dimension powder pattern relative to ideal spectrum.[11,40] In this case, extraction of reliable information from the $\omega_2/2\pi$-dimension lineshape requires numerical simulations considering effects from the time-modulated first-order quadrupolar interactions in course of the rf pulses. Intuitively, this requirement appears most relevant for the MQ-QCPMG-MAS experiments detecting the $\omega_2/2\pi$ spectrum through a series of finite refocusing pulses, although the weak rf field strength should ensure almost isotropic behavior during B and C of the Figure 1 pulse sequence (vide supra).

The relevance of considering the effects of finite rf pulses becomes evident from the $\omega_2/2\pi$ sections through the various isotropic resonances in the ^{87}Rb MQ-QE-MAS and MQ-QCPMG-MAS spectra of RbNO$_3$ in Figures 4b and 5b, respectively. The sections through the experimental spectra shown in the left columns of Figures 4b and 5b may be reproduced fairly well by the numerically exact simulations shown in the corresponding center columns. The simulated spectra were obtained by iterative fitting of $\omega_2/2\pi$ sections from the experimental MQ-QCPMG-MAS spectrum using the formalism already described under consideration of finite rf pulse effects. The resulting parameters are summarized in Table 1 along with parameters from recent ^{87}Rb solid-state NMR studies of RbNO$_3$. Using the optimum parameters to calculate the same $\omega_2/2\pi$ sections under the assumption of ideal single-pulse excitation leads to the simulations shown in the right-hand columns of Figures 4b and 5b. The differences between the two sets of simulations reveal that accurate extraction of the anisotropic interaction parameters requires appropriate consideration of finite rf pulse effects. In this context, it is important to note that the distortions originate from the first two MQ pulses in the experiment whereas the following *z*-filter and refocusing pulses may, to a good approximation, be considered ideal in their behavior (vide supra).

TABLE 1: Magnitudes of Quadrupolar Coupling Tensors and Isotropic Chemical Shifts for ^{87}Rb in RbNO$_3$

site	C_Q (MHz)	η_Q	δ_{iso} (ppm)[a]	method
Rb(1)	1.80	0.30	−27.5	MQ-QCPMG-MAS
	1.69	0.25	−27.5	MQ-MAS[39]
	1.68	0.2	−27.4	MQ-MAS[32]
	1.83	0.12	−26.2	DAS[42]
Rb(2)	2.00	0.97	−28.7	MQ-QCPMG-MAS
	2.01	0.94	−28.9	MQ-MAS[39]
	1.94	1.0	−28.5	MQ-MAS[32]
	2.07	1.0	−26.8	DAS[42]
Rb(3)	1.67	0.63	−32.0	MQ-QCPMG-MAS
	1.71	0.55	−31.4	MQ-MAS[39]
	1.72	0.5	−31.3	MQ-MAS[32]
	1.85	0.48	−30.9	DAS[42]

[a] Isotropic chemical shifts on the δ-scale are referenced to a 1.0 M solution of RbNO$_3$.

The distortion of the MQ-QE-MAS powder pattern or the MQ-QCPMG-MAS spin-echo sideband envelope strongly depends on $|\omega_Q/\omega_{rf}|$ and ω_r. To illustrate this aspect, Figure 6 shows a series of $\omega_2/2\pi$ projections calculated for MQ-QCPMG-MAS experiments using different rf field strengths and sample spinning conditions for a powder of spin $I = 3/2$ nuclei with $\omega_Q/2\pi$ values of 167 kHz ($C_Q = 2$ MHz) and 333 kHz ($C_Q = 4$ MHz) at a Larmor frequency of 98.14 MHz. For comparison, the upper row of Figure 6 contains the corresponding QCPMG-MAS spectra calculated under the assumption of ideal rf pulse conditions. From these spectra it is evident that the spectra with the smallest values of $|\omega_Q/\omega_{rf}|$ (i.e., smallest C_Q and largest ω_{rf}) most closely resemble an ideal second-order spin-echo sideband spectrum, whereas very significant distortions are observed for larger values of this ratio. The effect of the sample spinning frequency becomes apparent by comparing the two left-most columns in Figure 6, indicating that even in case of low $|\omega_Q/\omega_{rf}|$ ratios, this effect has to be considered. We note that part of the differences originate from the different optimum t_{3Q} and t_{31} values. Independently of this effect, it can be concluded that the highest possible rf field strengths are highly desirable and that with an rf field strength of 200 kHz, essentially undistorted traces are observed even for $\omega_Q/2\pi = 333$ kHz. This rather high value for the quadrupole splitting promises a wide range of applicability of the MQ-QCPMG-MAS experiment when strong rf fields are available.

Equipped with accurate parameters for the quadrupolar coupling interactions and the isotropic shifts in the $\omega_1/2\pi$-

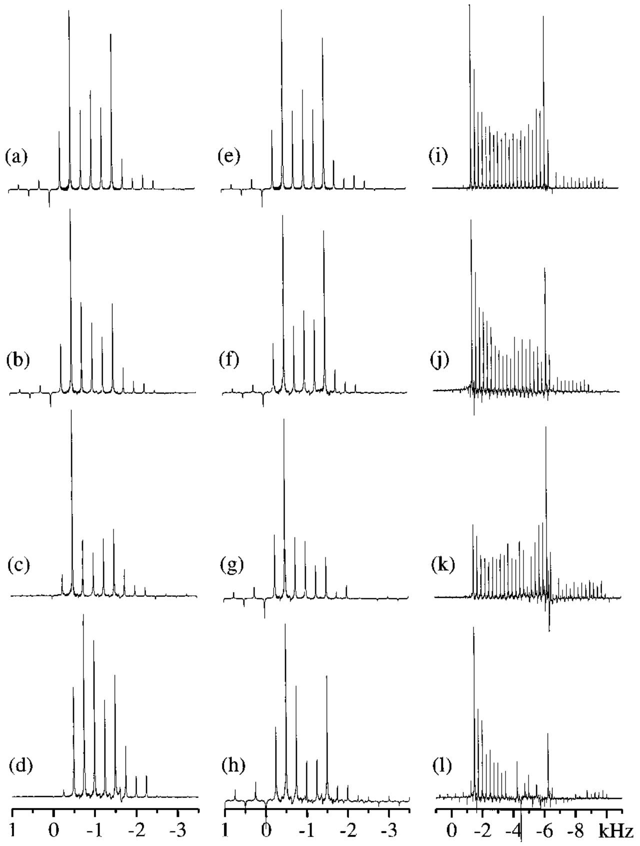

Figure 6. Calculated (a, e, i) QCPMG-MAS spectra and (b−d, f−h, j−l) $\omega_2/2\pi$ sections from MQ-QCPMG-MAS spectra. The QCPMG-MAS spectra were calculated under the assumption of ideal rf pulse excitation and the MQ-QCPMG-MAS spectra calculations used finite rf pulse conditions with $\omega_{rf}/2\pi$ values of (b, f, j) 200, (c, g, k) 100, and (d, h, l) 50 kHz. The spectra used $I = 3/2$, $\omega_0/2\pi = -98.14$ MHz, $\eta_Q = 0.0$, $\delta_{iso} = 0.0$ ppm, $\omega_{rf2}/2\pi = 25$ kHz, $\tau_a = 4.0$ ms, $M = 20$, $\tau_d = 0.1$ ms. The spectra correspond to C_Q values of (a−h) 2 and (i−l) 4 MHz and $\omega_r/2\pi$ values of (a−d) 4.9 ($\tau_1 = \tau_2 = 204.08$ μs, $\tau_3 = \tau_4 = 35.8$ μs) and (e−l) 11.8 ($\tau_1 = \tau_2 = 84.75$ μs, $\tau_3 = \tau_4 = 28.9$ μs) kHz. The MQ-QCPMG-MAS calculations used optimum t_{3Q} and t_{31} pulse lengths (in μs) of (b) 34.5, 42.5, (c) 17.5, 66.0, (d) 3.5, 82.0, (f) 34.5, 30.5, (g) 12.5, 42.5, (h) 3.5, 57.0, (j) 103.5, 59.0, (k) 12.5, 11.5, and (l) 8.5, 84.75. All spectra were apodized by a Lorentzian weighting of 10 Hz.

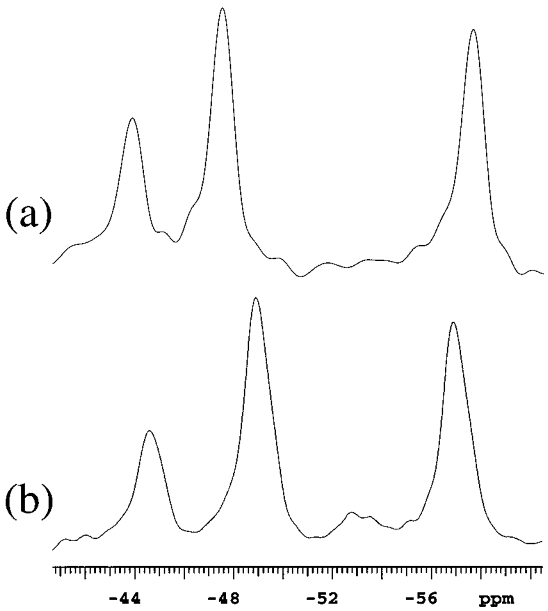

Figure 7. Calculated (a) and experimental (b) $\omega_1/2\pi$ projections of the ^{87}Rb MQ-QCPMG-MAS spectrum of RbNO$_3$. The simulations used parameters identical to those in Figure 5 and Table 1. The calculated $\omega_1/2\pi$ trace is apodized by a Lorentzian weighting of 100 Hz.

dimension extracted from the 2D spectra in Figures 4 and 5, it is a simple matter to determine the isotropic chemical shifts for the various ^{87}Rb sites of RbNO$_3$. The specific values are included in Table 1. Furthermore, using the quadrupolar interaction parameters and the actual pulse widths/amplitudes, it is possible to determine the populations of the various sites from the intensities observed in the projection onto the $\omega_1/2\pi$ axis. This determination may be accomplished using excitation and reconversion profiles as in Figures 2 and 3 or by specific calculation of the $\omega_1/2\pi$ projection of the 2D spectrum. In addition, the latter approach will provide a direct test on the isotropic chemical shift values extracted from the $\omega_2/2\pi$ dimension of the 2D spectrum. Both aspects are illustrated in Figure 7, which compares experimental and calculated $\omega_1/2\pi$ projections for the ^{87}Rb MQ-QCPMG-MAS spectrum of RbNO$_3$. The two spectra in Figure 7 reveal that the calculated δ'_{iso} values are within ±1 ppm from the experimental values. Assuming an ideal 1:1:1 population of the three sites, in accordance with the crystal structure, the calculated intensities for the Rb(1), Rb(2), and Rb(3) sites are 1.00:0.55:0.94, whereas the corresponding experimental intensities are 1.00:0.46:0.86. In both cases, the most intense resonance in the $\omega_1/2\pi$ dimension was assigned the value 1.00. This assignment implies that experimentally, the populations of the various sites are 1.00: 0.84:0.91, which are fairly close to the values expected from theory.

Conclusion

In conclusion, we have demonstrated that it is practically feasible to numerically simulate and iteratively fit experimental MQ-QE-MAS and MQ-QCPMG-MAS spectra to establish optimum experimental conditions and obtain accurate parameters describing the quadrupolar coupling interaction, the isotropic chemical shifts, and the relative populations of different quadrupolar spin sites. By explicit calculation of transfer efficiencies, we have demonstrated that the sensitivity of the simple two-pulse MQ-MAS experiment may be about doubled using significantly longer excitation and reconversion pulses than typically recommended. In addition to this comes an order of magnitude in sensitivity obtained using the MQ-QCPMG-MAS experiment splitting the second-order powder patterns in the $\omega_2/2\pi$ dimension of the 2D spectrum into distinct spin-echo sidebands. For MQ-MAS as well as MQ-QCPMG-MAS experiments, we have demonstrated how numerically exact simulation and iterative fitting of the lineshape or sideband pattern in the anisotropic dimension may be used to obtain accurate parameters for the involved isotropic and anisotropic interaction parameters as well as the relative site populations. All these aspects are practically important and are anticipated to find direct application in future MQ-MAS studies.

Acknowledgment. The use of the Varian INOVA-300 NMR spectrometer, sponsored by by the Danish Natural Science Council, at the Instrument Centre for Solid-State NMR Spectroscopy, University of Aarhus, is acknowledged. The authors thank Mads Bak for helpful discussions regarding numerical simulation of multiple-quantum transfers.

References and Notes

(1) Frydman, L.; Harwood, J. S. *J. Am. Chem. Soc.* **1995**, *117*, 5367.
(2) Llor, A.; Virlet, J. *J. Chem. Phys.* **1988**, *152*, 248.

(3) Chmelka, B. F.; Mueller, K. T.; Pines, A.; Stebbins, J.; Wu, Y.; Swanziger, J. W. *Nature* **1989**, *339*, 42.

(4) Mueller, K. T.; Sun, B. Q.; Chingas, G. C.; Zwanziger, J. W.; Terao, T.; Pines, A. *J. Magn. Reson*. **1990**, *86*, 470.

(5) Samoson, A.; Lippmaa, E.; Pines, A. *Mol. Phys.* **1988**, *65*, 1013.

(6) Wu, Y.; Sun, B. Q.; Pines, A.; Samoson, A.; Lippmaa, E. *J. Magn. Reson.* **1990**, *89*, 297.

(7) Wu, G.; Rovnyank, D; Sun, B.; Griffin, R. G. *Chem. Phys. Lett.* **1995**, *249*, 210.

(8) Medek, A.; Harwood, J. S.; Frydman, L. *J. Am. Chem. Soc.* **1995**, *117*, 12779.

(9) Fernandez, C.; Amoureux, J. P. *Chem. Phys. Lett.* **1995**, *242*, 449.

(10) Wu, G.; Rovnyank, D.; Griffin, R. G. *J. Am. Chem. Soc.* **1996**, *118*, 9326.

(11) Lim, K. H.; Grey, C. P. *Solid State NMR* **1998**, *13*, 101.

(12) Marinelli, L.; Medek, A.; Frydman, L. *J. Magn. Reson.* **1998**, *132*, 88.

(13) Ding, S.; McDowell, C. A. *J. Magn. Reson.* **1998**, *135*, 61.

(14) Kentgens, A. P. M.; Verhagen, R. *Chem. Phys. Lett.* **1999**, *300*, 435.

(15) Madhu, P. K.; Goldbourt, A.; Frydman, L.; Vega, S. *Chem. Phys. Lett.* **1999**, *307*, 41.

(16) Vosegaard, T.; Larsen, F. H.; Jakobsen, H. J.; Ellis, P. D.; Nielsen, N. C. *J. Am. Chem. Soc.* **1997**, *119*, 9055.

(17) Carr, H. Y.; Purcell, E. M. *Phys. Rev.* **1954**, *94*, 630.

(18) Meiboom, S.; Gill, D. *Rev. Sci. Instrum.* **1958**, *29*, 688.

(19) Larsen, F. H.; Jakobsen, H. J.; Ellis, P. D.; Nielsen, N. C. *J. Phys. Chem.* **1997**, *A 101*, 8597.

(20) Larsen, F. H.; Jakobsen, H. J.; Ellis, P. D.; Nielsen, N. C. *J. Magn. Reson.* **1998**, *131*, 144.

(21) Larsen, F. H.; Jakobsen, H. J.; Ellis, P. D.; Nielsen, N. C. *Mol. Phys.* **1998**, *95*, 1185.

(22) Samoson, A.; Lippmaa, E. *J. Magn. Reson.* **1989**, *84*, 410.

(23) Rose, M. E. *Elementary Theory of Angular Momentum*; Wiley: New York, 1957.

(24) Brown, S. P.; Heyes, S. J.; Wimperis, S. *J. Magn. Reson., Ser. A* **1996**, *119*, 280.

(25) Amoureux, J.-P.; Fernandez, C.; Steuernagel, S. *J. Magn. Reson., Ser. A* **1996**, *123*, 116.

(26) Brown, S. P.; Wimperis, S. *J. Magn. Reson., Ser. A* **1997**, *128*, 42.

(27) Solomon, I. *Phys. Rev.* **1958**, *110*, 61.

(28) Weisman, I. D.; Bennett, L. H. *Phys. Rev.* **1969**, *181*, 1341.

(29) Davis, J. H.; Jeffrey, K. R.; Bloom, M.; Valic, M. I.; Higgs, T. P. *Chem. Phys. Lett.* **1976**, *42*, 390.

(30) Dyson, F. J. *Phys. Rev.* **1949**, *75*, 486.

(31) Zaremba, S. K. *Annali di matematica pura ed applicata* **1966**, *73*, 293.

(32) Massiot, D.; Touzo, B.; Trumeau, D.; Coutures, J. P.; Virlet, J.; Florian, P.; Grandinetti, P. J. *Solid State NMR* **1996**, *6*, 73.

(33) Amoureux, J.-P.; Pruski, M.; Lang, D. P.; Fernandez, C. *J. Magn. Reson.* **1998**, *131*, 170.

(34) Vega S.; Naor, Y. *J. Chem. Phys.* **1981**, *75*, 75.

(35) Nielsen, N. C.; Bildsøe, H.; Jakobsen, H. J. *Chem. Phys. Lett.* **1992**, *191*, 205.

(36) Nielsen, N. C.; Bildsøe, H.; Jakobsen, H. J. *J. Magn. Reson.* **1992**, *97*, 149.

(37) Massiot, D. *J. Magn. Reson., Ser. A* **1996**, *122*, 240.

(38) Abragam, A. *The principles of nuclear magnetism*; Clarendon: Oxford; 1961.

(39) Hanaya, M.; Harris, R. K. *J. Phys. Chem.* **1997**, *A101*, 6903.

(40) Charpentier, T.; Fermon, C.; Virlet, J. *J. Chem. Phys.* **1998**, *109*, 3116.

(41) Amoureux, J.-P.; Fernandez, C.; Frydman, L. *Chem. Phys. Lett.* **1996**, *259*, 347.

(42) Baltisberger, J. H.; Gan, S. L.; Wooten, E. W.; Chang, T. H.; Mueller, K. T.; Pines, A. *J. Am. Chem. Soc.* **1992**, *114*, 7489.

(43) Bodenhausen, G.; Kogler, H.; Ernst, R. R. *J. Magn. Reson.* **1984**, *58*, 370.